MHD stability analysis of diagnostic optimized configuration shots in JET

S Saarelma[1], V Parail[2], Y Andrew[2], E de la Luna[3], A Kallenbach[4], M Kempenaars[5], A Korotkov[2], A Loarte[6], J Lönnroth[1], P Monier-Garbet[7], J Stober[4], W Suttrop[4] and Contributors to the EFDA-JET Workprogramme[8]

[1] Helsinki University of Technology, Euratom-TEKES Association, FIN-02015 HUT, Finland
[2] EURATOM/UKAEA Fusion Association, Culham Science Centre, Abingdon, Oxfordshire OX14 3DB, UK
[3] Associacion EURATOM-CIEMAT para Fusion, Avenida Complutense 22, E-28040 Madrid, Spain
[4] MPI für Plasmaphysik, EURATOM Association, D-85748 Garching, Germany
[5] FOM-Rijnhuizen, Ass. Euratom-FOM, TEC, PO Box 1207, 3430 BE Nieuwegein, Netherlands
[6] EFDA, CSU-Garching, Garching, Germany
[7] Association EURATOM-CEA, CEA Cadarache, DRFC, 13108, Saint-Paul-Lez-Durance, France

E-mail: samuli.saarelma@hut.fi

Abstract

The plasma edge MHD stability is analysed for several JET discharges in the diagnostic optimized configuration. The stability analysis of Type I ELMy plasmas shows how after an edge localized mode (ELM) crash the plasma edge is deep in the stable region against low- to intermediate-n peeling–ballooning modes. As the pressure gradient steepens and the edge current builds up, the plasma reaches the low- to intermediate-n peeling–ballooning mode stability boundary just before the ELM crash. Increasing the plasma fuelling by gas puffing makes the second stability access against high-n ballooning modes narrower until it closes completely and the ELMs change from Type I to Type III. Reducing the plasma heating has a similar effect. Increasing the safety factor at the plasma edge improves the stability against low- to intermediate-n modes allowing steeper pressure gradients to develop before an ELM crash.

(Some figures in this article are in colour only in the electronic version)

1. Introduction

The high-confinement-mode (H-mode) in present day tokamaks is regularly accompanied by short bursts of plasma energy and particles. These edge localized modes (ELMs) create

---

[8] See annex of J Pamela *et al* 2001 Overview of recent JET results and future perspectives *Fusion Energy 2000: Proc. 18th Int. Conf. (Sorrento, 2000)* (IAEA: Vienna).

high heat loads on the divertors and can cause significant erosion. For an estimate of this erosion in a future tokamak reactor operating in H-mode, it is necessary to understand the ELM phenomenon. This would also allow us to analyse the necessity and usability of actual techniques of ELM mitigation and control in such a device.

The main issues in the control of the ELMs are the size of a single ELM crash [1] and the confinement degradation caused by the ELMs. The ELM size is generally measured as a drop in plasma diamagnetic energy during an ELM [2]. In this paper, two types of ELMs, Type I and Type III, are considered. Since no pure Type II ELMs have been observed in JET [3], they are excluded from the analysis. Type I ELMy plasmas have good confinement properties, but the ELMs are generally large in size, while the Type III ELMs are smaller, but the plasma performance is worse than in Type I ELMy plasma.

The generally accepted model for ELMs is that they are triggered by a combination of two MHD instabilities, low- to intermediate-n peeling–ballooning modes and high-n ballooning modes [4, 5]. The peeling–ballooning modes are driven by the current in the edge region and the ballooning modes by the pressure gradient. The stability against these instabilities governs the behaviour of the edge plasma. The peeling–ballooning model for ELMs has been studied with several experiments: ASDEX-Upgrade [6], DIII-D [7] and JT-60U [8]. In all these studies, edge localized low- to intermediate-n peeling–ballooning instabilities have been found in Type I ELMy plasmas agreeing with the predictions of the model.

Several experiments have been carried out on the JET tokamak to study ELMs [9, 10]. However, the recent JET discharges in the diagnostic optimized configuration (DOC) allow gradients in the edge region to be resolved and permit detailed systematic stability analysis of the edge region using the experimental density and temperature profiles. A detailed description of the DOC discharges is given in [11].

In this paper, we show the MHD stability analysis results for a series of DOC discharges. We analyse scans of gas puffing, edge safety factor and heating power done in DOC and show how the edge stability changes with these parameters. Comparing the stability results with the observed ELM behaviour gives insight into the physics of the triggering mechanism of the ELMs. In the DOC-discharges investigated, the shape of the plasma has been set to give the best possible resolution from the edge diagnostics. The triangularity of this configuration varies from 0.27 (DOC-L) to 0.32 (DOC-U).

2. Equilibrium reconstruction of experimental plasmas

In the equilibrium reconstruction that is needed for the stability analysis, we use experimental temperature and density profiles and calculate the ohmic and bootstrap currents self-consistently using the profiles. This method provides us with equilibria that represent the actual experimental equilibria as accurately as possible and allows us to study the edge stability properties of the experimental plasmas.

We use edge LIDAR Thomson scattering [12, 13] and an ECE radiometer [15] for the edge electron temperature profiles. In addition, we assume $T_e = T_i$ and use the ion temperature data, obtained using edge charge exchange recombination spectroscopy (CXRS), as extra information about the electron temperature at the top of the H-mode pedestal. After fitting the electron temperature profile, the ion temperature profile is set by the same assumption ($T_i = T_e$). It must be noted that this assumption can overestimate the steepness of the edge ion temperature gradient. The edge LIDAR system is used to obtain the edge temperature gradient, and the pedestal top is obtained from ECE and CXRS. The combination of all three diagnostics gives an accurate temperature profile in the entire edge region.
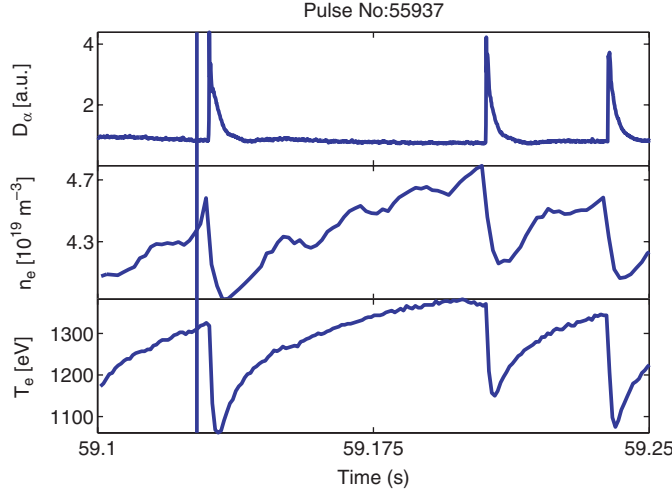
Figure 1. The time evolution of the divertor D_α-signal, edge density and temperature in a typical JET type I ELMy discharge (#55937). The density data are from the edge interferometer and the temperature from the ECE channel at the pedestal top. The vertical line represents the time of the edge LIDAR measurement.

The core temperature is obtained from the core LIDAR Thomson scattering [14]. The core LIDAR data has larger error bars, but since the accuracy of the core profile is not crucial for the edge stability, larger errors in the core profile can be tolerated without affecting the edge stability analysis results.

From the experimental data we create the temperature profiles for the equilibrium reconstruction by fitting a function

$$T_0(1 - \rho^a)^b - T_{\text{ped}} \tanh\left(\frac{\rho - d}{c}\right) + T_{\text{sep}}, \tag{1}$$

where ρ is the square root of the normalized toroidal flux, T_0, T_{ped} and T_{sep} are parameters used to set the pedestal, core and separatrix temperatures, and a, b, c and d are parameters for the shape of the profile.

The edge density profile is obtained by combining the data from the edge LIDAR and lithium beam diagnostics. As with temperature, we use core LIDAR to get the core density profile. The density profile used in the equilibrium reconstruction is obtained by fitting a function

$$n_0(1 - \rho^a)^b - n_{\text{ped}} \tanh\left(\frac{\rho - d}{c}\right) + n_{\text{sep}}, \tag{2}$$

where n_{ped}, n_0 and n_{sep} are used to set the pedestal, core and separatrix densities. Additionally, we use the line-averaged density from the vertical interferometer at the radius of 3.75 m as a constraint for the edge region density fit. Naturally, the fitting parameters (a, b, c and d) for density differ from those of the temperature.

The repetition rate of the edge LIDAR laser is 1 Hz. To obtain the most relevant data for the stability analysis, we select the time point in each pulse that is the closest to an ELM (usually <20 ms prior to an ELM crash). Figure 1 shows a typical time evolution of the D_α signal, edge density and temperature in the Type I ELMy plasma. The vertical line shows the time point of the edge LIDAR profile. As can be seen, the temperature is reasonably steady prior to an ELM, and there is only a small error in using the edge LIDAR that is within 20 ms

from the ELM crash as the temperature profile at the moment when the ELM is triggered. The pedestal density growth does not saturate to a steady-state value in the same way as the temperature, but the line-averaged density at 20 ms prior to an ELM is only about 5% lower than the value at the ELM crash, which is smaller than the error margin in the edge LIDAR system. Therefore, the error in the edge density profile due to being measured 20 ms before the crash does not significantly affect the results. In type III ELMy pulses, the temporal variation of the profiles (especially density) does not correlate with the D_α signal. In these cases, we use several time points (within the flat top of NBI heating) of the edge LIDAR system and average within them.

Unfortunately, the ECE, the edge CXRS and the edge LIDAR do not always match. Especially, the T_e from ECE is systematically shifted inwards with regard to LIDAR and edge CXRS. This is most likely due to an error in the flux mapping at the edge. The ECE system is poloidally located horizontally on the low field side slightly below the equatorial plane, CXRS covers the low field side edge region, while the edge LIDAR measures the data near the x-point. The lithium-beam measurements are done at the top of the plasma along a vertical beam trajectory at $R = 3.252$ m.

A good estimate for the separatrix electron temperature is given by the balance between the power crossing the separatrix and the parallel heat conduction to the divertors. In JET H-modes, this value is usually about 100–140 eV. Since for most of the discharges the edge LIDAR gives a profile that has a separatrix temperature in this range, it is assumed to be correct. Therefore, ECE needs to be shifted radially by about 5% of the poloidal flux outwards to match the profiles. The shift has been used in the fitting, even in the cases where no edge CXRS is available. For discharges where the edge LIDAR value for the separatrix temperature is several hundreds of electron volts, edge LIDAR is shifted inwards to match the value set by the power balance. The edge LIDAR shifts are usually very small, about 1% of the poloidal flux, and do not affect the steepness of the pressure gradient, but only its position. In some cases, the lithium beam profile is also shifted to match it with the edge LIDAR density profile. These shifts are also about 1% of the poloidal flux.

Once the radial shift is applied to the ECE data, T_e profiles measured by ECE and edge Thomson scattering are in reasonable agreement for $\rho < 1$ (see figure 2). However, a pronounced feature of enhanced ECE radiation temperature (radiation 'hump', denoted by an arrow in the figure) appears at channels located outside the separatrix. At the plasma edge the optical depth can vary greatly (from less than 0.1 to 10) and care must be taken in the interpretation of edge ECE measurements in terms of local electron temperatures. The mechanism by which this radiation hump is generated is not well understood [16], but its shape can be used to estimate the optical depth profile in the edge region. In these plasmas with steep edge gradients, the transition from optically thin to optically thick occurs over a few centimetres, which corresponds to one or two radiometer channels. In the data shown in figure 2, the minimum just before the hump corresponds to the lowest frequency channel for which the thermal plasma is optically thick. Consequently, the ECE data outside the separatrix have not been taken into account when performing the profile fittings. A typical global and edge fitting of the profiles is shown in figure 2. The fitting is done for the discharge #55937 at 59.126 s, that is 2 ms before an ELM crash. The profiles of all analysed discharges and the radial shifts used in the fitting are collected in the appendix.

We use JETTO [17] to solve the self-consistent equilibrium including the bootstrap current for the fitted profiles. The effective charge Z_{eff} is assumed to be constant throughout the plasma. The value of Z_{eff} is calculated using the line-averaged density, bremsstrahlung signal, peak electron temperature and the path length through the plasma. In the discharges studied Z_{eff} varies in the range from 1.8 to 2.5. The plasma shape is obtained from the EFIT [18]
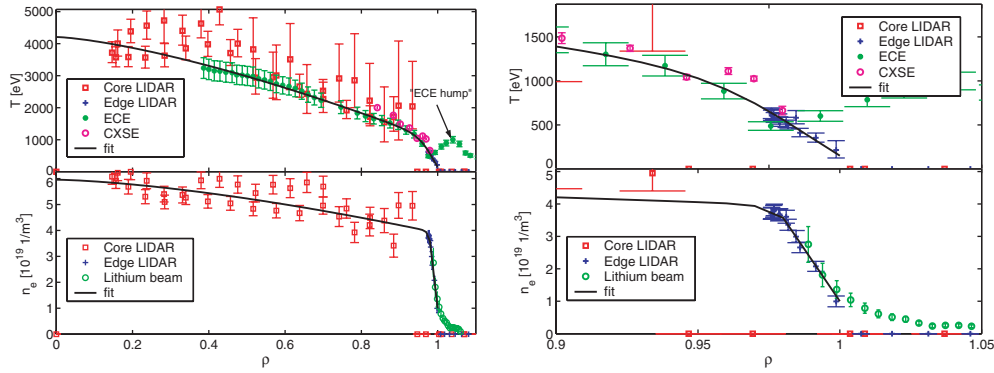
Figure 2. A fitting of the radial temperature and density profiles in the entire plasma and in the edge region for the pulse #55937 at 59.126 s (2 ms before an ELM). The profiles are plotted as a function of the normalized toroidal flux. The ECE data points have been shifted 5 cm outwards to get better agreement with the edge LIDAR and CXRS. The lithium-beam data points are shifted 0.9 cm outwards for the same reason. The arrow shows the 'hump' in ECE data. It is ignored in the fitting.

reconstruction using magnetic measurements. In the JETTO equilibrium calculations, we assume that the current has reached a steady state. The total current is composed of inductively driven current, which follows the plasma conductivity profile, and the bootstrap current, which is driven by the density and temperature gradients. In the edge region that covers most of the ELM physics, the bootstrap current clearly dominates the inductively driven current.

3. Stability analysis

3.1. Stability analysis methods

We analyse the stability of the equilibria using the MISHKA-1 [19] code for the low- to intermediate-n peeling–ballooning modes. Using the HELENA [20] equilibrium code and the plasma profiles and shape from JETTO equilibrium, we re-calculate the equilibria for MISHKA-1, which require the equilibrium in the straight field line co-ordinate system. HELENA also solves for the stability against the $n = \infty$ ballooning modes.

In the MISHKA stability analysis, the toroidal mode numbers are varied from 3 to 10. The mode number choice was based on the reported experimental observation of the ELM-precursor mode numbers ($n = 1$–14 in [21] and [22]). Even higher (up to 40) mode numbers were investigated for a few selected cases, but since they showed no qualitative difference to $n = 10$ (except for approaching the $n = \infty$ ballooning mode boundary at high shear), and required more computational resources ($\sim n^2$), they were left out from the systematic studies. Figure 3 shows an example of the $n = 10$ peeling–ballooning instability from MISHKA analysis for the discharge #55937 just before an ELM. Both the radial structure of the mode using Fourier harmonics and the two-dimensional contour plot of the mode amplitude are plotted.

We solve only one JETTO equilibrium for each pulse. This is called the operational point in the stability analysis as it represents the equilibrium of the experimental plasma. In the input for the HELENA equilibrium code, we scale the pressure gradient and the current density in the edge region to find the stability boundaries around the operational point. The scaling is
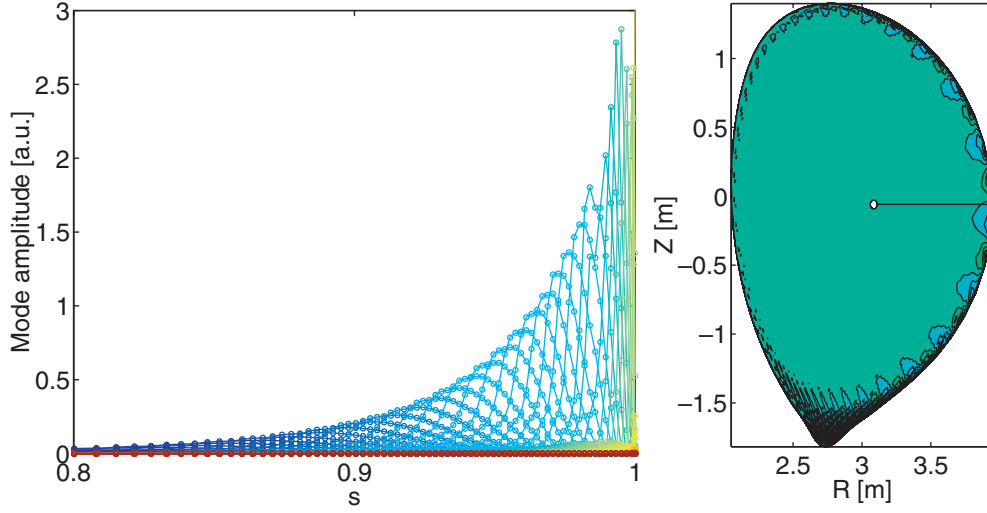
Figure 3. Fourier decomposition as a function of the normalized radius s $(=\sqrt{\psi})$ and the contour plot of the radial displacement amplitude for the $n = 10$ peeling–ballooning instability in discharge #55937 just before an ELM.

done with a step function in the entire pedestal region, i.e.:

$$f(\rho) = f(\rho)_{\text{experimental}}, \qquad \text{when } \rho < 0.95, \tag{3}$$

$$f(\rho) = C \cdot f(\rho)_{\text{experimental}}, \qquad \text{when } \rho > 0.95, \tag{4}$$

where C is a constant and f is either p' or $j_{\parallel}$. The scaling does not affect the width of the pressure pedestal, only the height. The stability boundaries along with the operational point can then be plotted for a specific flux surface in a diagram with the normalized pressure gradient α $(=2\mu_0 R q^2 (\mathrm{d}p/\mathrm{d}r)/B^2)$, evaluated at the outer mid-plane, and the magnetic shear s $(=(\mathrm{d}q/\mathrm{d}r)/(r/q))$ as the x- and y-axes, respectively.

In order to obtain error margins for the operational point, the experimental profiles are fitted with curves that have the flattest and steepest possible gradients that can be fitted while staying within error bars of the experimental data points. An equilibrium is solved for both the flat and steep gradient fits. The values of α and s in these equilibria are used as error bars for the operational point.

3.2. Stability within an ELM cycle

We first investigate how the edge stability varies during an ELM cycle. As was shown in figure 1, between the ELMs, the pedestal density and temperature increase. Then, during the ELM crash, they both collapse. To obtain the maximum variation within a single discharge, we compare the stability just before a Type I ELM and right after it. The selected discharge (#55937) is a typical Type I ELMy discharge in DOC-L and has medium triangularity, $\delta = 0.27$, and the following global plasma parameters: plasma current $I_{\mathrm{p}} = 2.0\,\mathrm{MA}$, toroidal magnetic field $B_{\mathrm{t}} = 2.4\,\mathrm{T}$, NBI heating power $P_{\mathrm{NBI}} = 12.2\,\mathrm{MW}$ and density $\langle n_{\mathrm{e}}\rangle/n_{\mathrm{GW}} = 0.71$.

Since the edge LIDAR system operates at 1 Hz repetition frequency, it is impossible to use it to create temperature and density profiles before and after the same ELM. Therefore, we have to assume that the effects of ELMs on the profiles do not vary significantly between two ELMs and create the equilibria for the 'before ELM' and 'after ELM' plasmas using profiles
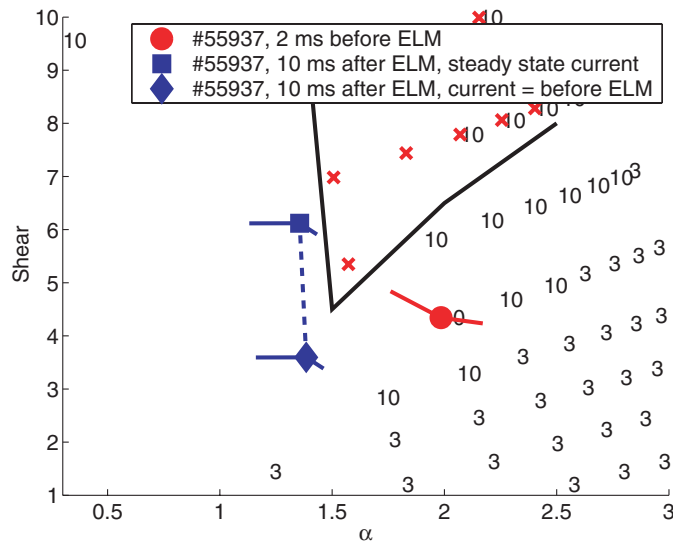
Figure 4. Stability diagram in shear–α space of a Type I ELMy discharge (#55937) before and after an ELM crash at $\psi = 0.985$. At 2 ms before the ELM (red circle), the current is assumed to have reached the steady state. After the ELM, two assumptions for the edge current are used: the current has diffused to steady state (blue square) and the current is the same as before an ELM crash (blue diamond). The numbers represent the mode number of the most unstable mode and the solid line and the crosses shows the $n = \infty$ ballooning mode stability boundary. The thin lines in the operational points show the error margins.

from different ELMs. From the point of view of edge stability, each ELM should behave more or less in the same way during the ELM cycle as long as the ELM type does not change.

Figure 4 shows how the operational point at the normalized poloidal flux surface $\psi = 0.985$ ($\approx$ position of the maximum pressure gradient) moves on the shear–α plane during the ELM cycle. The unstable region against low- to intermediate-n modes is marked by the number that represents the most unstable mode. The continuous black line shows the $n = \infty$ ballooning mode stability boundary. Just before an ELM, the plasma is deep in the second stable region against the $n = \infty$ ballooning mode, i.e. the low shear region, where α is not limited by an $n = \infty$ stability boundary. At the same time, the plasma has reached the low- to intermediate-n mode stability boundary. This instability then triggers the ELM. On the other hand, after the ELM crash, the edge pressure gradient flattens and the plasma returns deep into the stable region against low- to intermediate-n modes. If we assume that the current diffusion is sufficiently fast during an ELM crash, the current reaches its steady-state value after the ELM. Then, after an ELM, the pressure gradient becomes limited by the high-n ballooning mode stability boundary. Between the ELMs, the pressure gradient steepens and the bootstrap current builds up. This lowers the shear and the edge plasma moves deeper into the second stability region until it reaches the low- to intermediate-n stability limit, and an ELM is triggered again. If we assume that the current does not diffuse to a steady state during the ELM crash, but instead stays at the same level as before the crash, the second stability access remains open after the ELM crash. With this assumption, the high-n ballooning modes play no role in the Type I ELM cycle.

The discharge analysed here, #55937, will be the central point of the gas scan investigated in section 3.3.
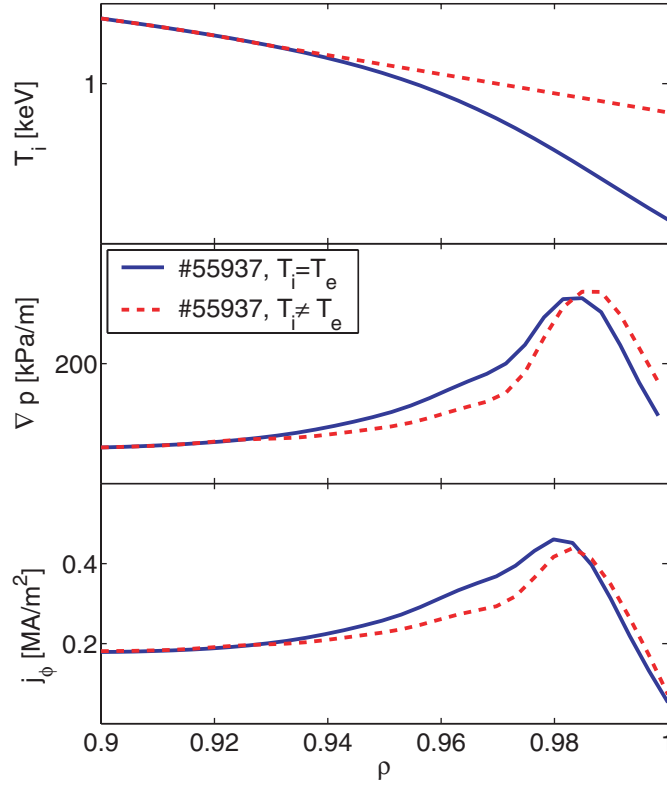
Figure 5. Fitted ion temperature, calculated total pressure gradient and toroidal current density profiles of discharge #55937 with two assumptions for the ion temperature profile: $T_i = T_e$ (——) and no edge ion transport barrier (- - - -).

In section 2 we noted that the assumption $T_i = T_e$ could overestimate the ion temperature gradient. Therefore, we studied the sensitivity of the edge stability of the 'before ELM' case to this assumption by creating an equilibrium with a T_i profile equal to T_e in the core and up to the pedestal top; in the pedestal region, however, $dT_i/d\rho$ is equal of that of the pedestal top. As shown in figure 5 the total edge pressure gradient and current density are only slightly affected. Consequently, the stability boundaries and the position of the operational point on the shear–α diagram change by less than the error bar shown in figure 4.

3.3. Gas puffing scan

To study the effects of external factors on the edge stability, we select well-diagnosed Type I and Type III ELMy discharges in various conditions and analyse their stability. One of the most used variations in the experiments is the gas puffing rate. This is studied with a theoretical model in [23]. Here, we study a series of JET discharges with identical plasma shape, current, toroidal field and heating, but varying gas puff rates. As the gas puff rate is increased, the ELM type changes from Type I ELMs to Type III ELMs. The increased gas puff leads to changes in the density and temperature profiles and, consequently, in the plasma equilibrium. Figure 6 shows the edge temperature, density, pressure gradient, parallel current density and magnetic shear of three equilibria with different gas puff rates. The edge pressure gradient
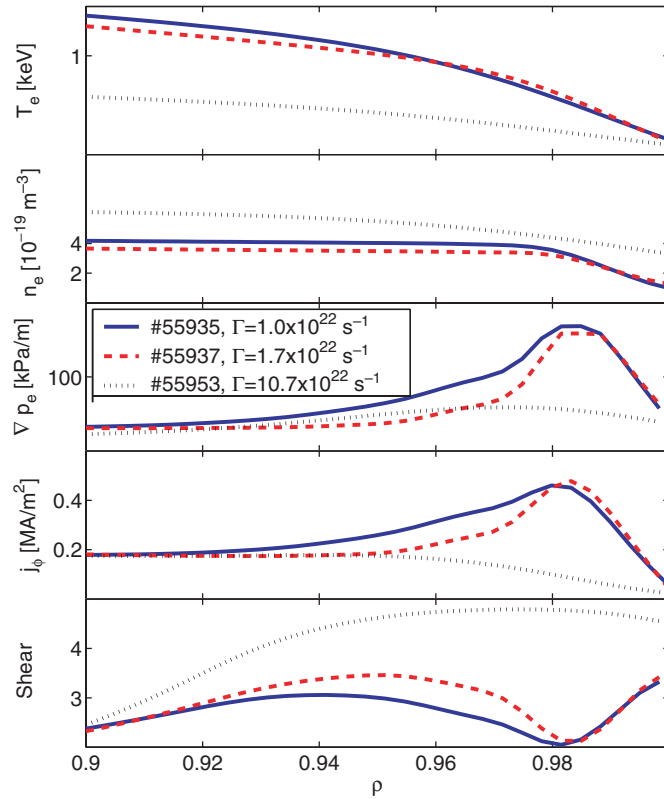
Figure 6. Fitted edge electron temperature, density profiles and calculated pressure gradient, toroidal current density and magnetic shear profiles for three levels of gas puffing: $1.0 \times 10^{22}\,\mathrm{s^{-1}}$ (——), $1.7 \times 10^{22}\,\mathrm{s^{-1}}$ (- - - -), $10.7 \times 10^{22}\,\mathrm{s^{-1}}$ (·····).

and current density in the Type III ELMy plasma is significantly lower than in the two Type I ELMy plasmas.

Figure 7 shows the $n = \infty$ ballooning stability boundary for the three levels of gas puffing rates. In the plot, α is increased from the equilibrium point without changing the magnetic shear until the stability boundary limit is found. If there is no stability limit, the boundary has not been drawn, and the pressure gradient is assumed to be able to grow in an unlimited fashion due to the high-n ballooning instability. This represents the 2nd stability access. It can be seen that the edge region loses the access to the 2nd stability as the gas puff rate increases. The reason is that the bootstrap current decreases and this increases the magnetic shear at the edge region closing the 2nd stability access.

On the other hand, the lowered bootstrap current improves the edge plasma stability against the low- to intermediate-n peeling–ballooning modes. Figure 8 shows the change in edge stability as the gas puffing is increased. The points with Type I ELMs (#55935, #55937) are just in the unstable region for low- to intermediate-n modes. On the other hand, the discharge with Type III ELMs (#55953) is clearly stable against these modes. As was already shown in figure 7, the pressure gradient in this discharge is limited by the high-n ballooning stability limit.

If we combine the stability analysis results for the low- and high-n modes, it seems likely that in the Type III ELMy plasmas the pressure gradient growth is limited to stay below the first
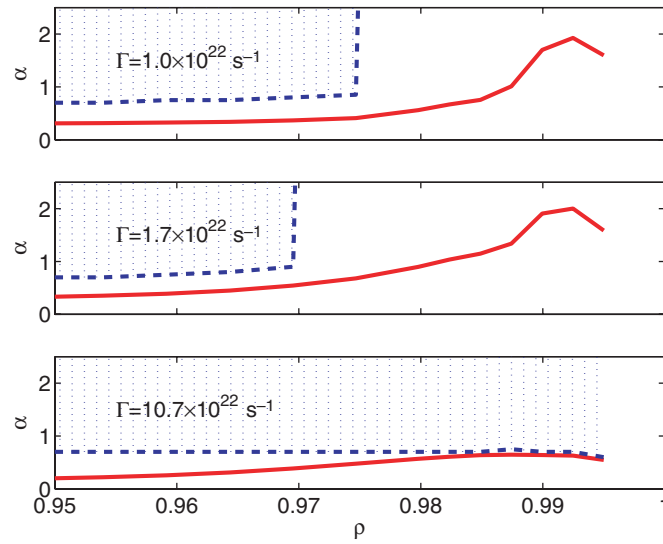
Figure 7. The normalized pressure gradient α and the $n = \infty$ ballooning stability boundary for three levels of gas puffing. The shaded area shows the region where an increase in pressure gradient without a change in magnetic shear makes the plasma unstable.
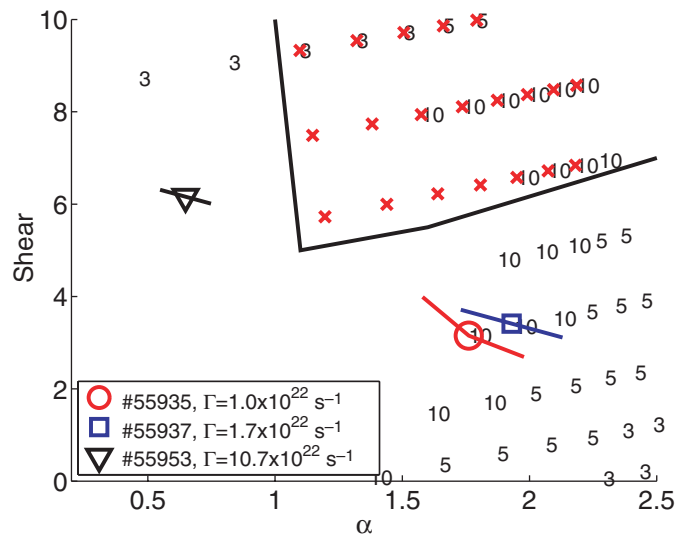

Figure 8. The α–shear stability diagram at $\psi = 0.99$ for three levels of gas puffing. The numbers represent the mode number of the most unstable mode and the solid line shows the $n = \infty$ ballooning stability boundary. The symbols with error bars show the experimental values of shear and α for each discharge.

$n = \infty$ ballooning mode stability boundary, but the Type I ELMy plasmas can access the second stability and are destabilized by the low- to intermediate-n modes at higher pressure gradients. The Type III ELMy discharges stay in the first stability region for the high-n ballooning modes because the conditions (high density, low temperature) prohibit the bootstrap current to build up sufficiently to lower the magnetic shear for the second stability access.
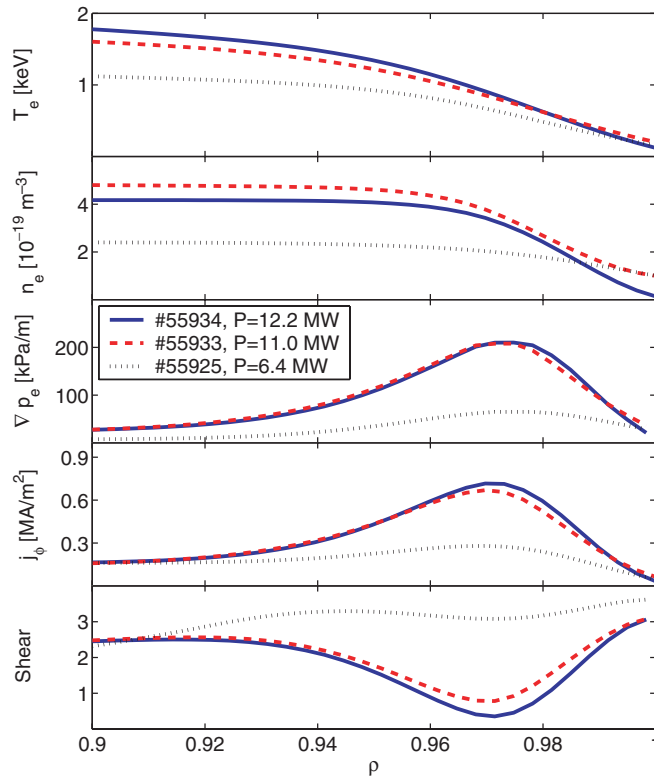
Figure 9. Fitted edge electron temperature, density profiles and calculated pressure gradient, toroidal current density and magnetic shear profiles for three levels of heating power: 12.2 MW (——), 11.0 MW (- - - -), 6.4 MW (······).

3.4. Power scan

The level of power injected into the plasma affects both the ELM type and the frequency of the ELMs. If the heating power into a Type III ELMy plasma is increased enough, the ELMs change to Type I. At the same time, the stability properties of the edge also change considerably. Figure 10 shows the operational point (at the steepest pressure gradient region, $\psi = 0.98$) in $s - \alpha$ space and the low-n stability limit for two Type I discharges (#55933, #55934) and one Type III discharge (#55925). All the discharges have the same shape (DOC-L), plasma current (2.0 MA) and magnetic field (2.4 T). No gas was puffed in any of the discharges during the NBI heating phase. The total heating power of the discharges was 6.4 MW for #55925, 11.0 MW for #55933 and 12.2 MW for #55934. Figure 9 shows the edge temperature, density, pressure gradient, parallel current density and magnetic shear of the three discharges with varying heating power. Again, the edge pressure gradient and current density in the Type III ELMy plasma is significantly lower than in the other two plasmas.

Just as in the gas scan, there is a significant difference in the edge stability between the Type I ELMy and Type III ELMy discharges. The Type I ELMy discharges are just over the low- to intermediate-n stability limit, while the Type III discharge is clearly in the stable region (figure 10). In this case, however, all discharges have second stability access for $n = \infty$ ballooning modes, but the pressure gradient in the Type III ELMy discharge is below the first stability limit and in the Type I ELMy discharges, above it.
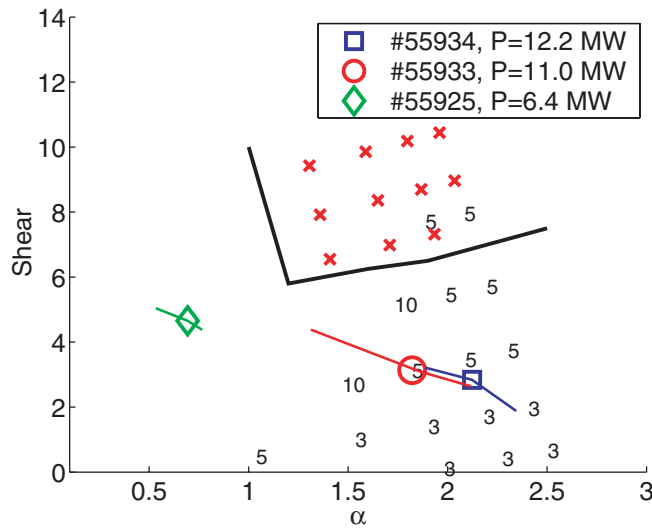
Figure 10. The α–shear stability diagram at $\psi = 0.98$ for three levels of NBI power. The numbers represent the mode number of the most unstable low- to intermediate-n mode, the solid line shows the $n = \infty$ ballooning mode stability boundary. The symbols with error bars show the experimental values of shear and α for each discharge.

Combining the power scan with the gas puffing scan, we can see that lowering the power and increasing the gas puff causes an almost identical effect in the edge stability. Both make the plasma more stable against the low-n peeling–ballooning modes, but, on the other hand, the operational point moves from the high-n ballooning mode second stability region to the first stability region. Type I ELMs are observed when the operational point of the edge plasma has a radially wide 2nd stability access for the high-n ballooning modes and the edge plasma is destabilized by the low- to intermediate-n peeling–ballooning modes. The Type I ELMs change to Type III ELMs when the high-n ballooning mode 2nd stability access becomes narrow in radius or closes completely. This transition mechanism is similar to that found for the transition from 'regular' Type I ELMs to 'small' Type I ELMs in DIII-D [7].

As mentioned in section 1 the Type III ELMy plasmas generally have poor confinement. In the discharges analysed in this paper, $\tau_E \approx 0.25$ s in plasmas with Type III ELMs and $\tau_E \approx 0.30$–0.45 s in plasmas with Type I ELMs. However, it is not clear, if the Type III ELMs are the cause of the poor confinement or that the plasma with poor confinement produces Type III ELMs. From the stability analysis it is not clear, what the triggering mechanism of Type III ELMs is.

3.5. Edge safety factor

The variation of the edge safety factor (q_{95}) also affects the ELM behaviour. The frequency of the ELMs increases and the ELMs get smaller with increasing q_{95}. For the stability analysis we choose three discharges (#55986, #55935 and #58809) with identical shapes (DOC-L), and same fuelling (1.0×10^{20} s^{-1}) and plasma current (2.0 MA). The toroidal magnetic field in these discharges is 1.8 T, 2.4 T and 3.0 T, respectively. The heating power is 12 MW in discharges #55986 and #55935, and 15 MW in #58809. All discharges have Type I ELMs, but the ELM frequency is lower in discharges with a low edge safety factor. As was shown in figure 10, the power level does not significantly affect the edge stability properties as long as
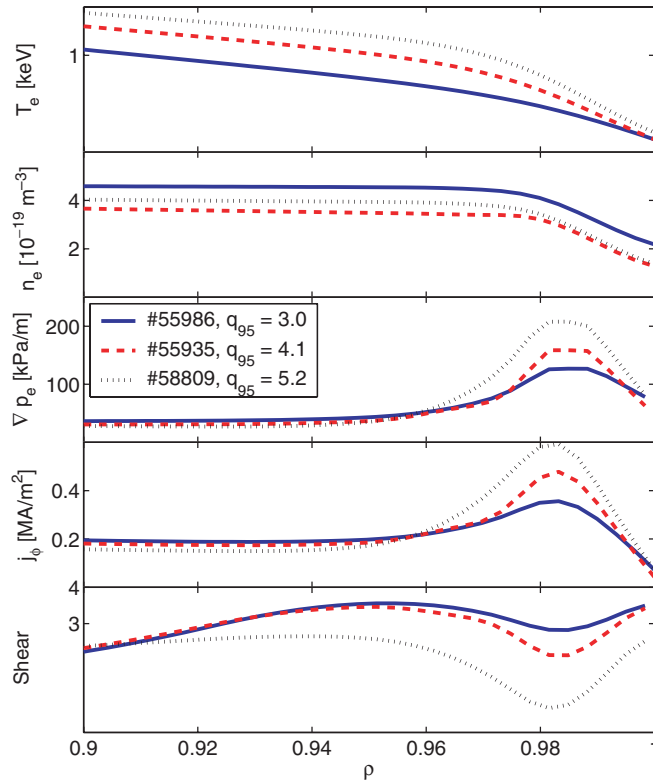
Figure 11. Fitted edge electron temperature, density profiles and calculated pressure gradient, toroidal current density and magnetic shear profiles for three levels of q_{95}: 3.0 (——), 4.1 (- - - -), 5.2 ($\cdots\cdots$).

the ELMs do not change from Type I to Type III. Therefore, the different power levels should not affect the results. The values of the edge safety factor (q_{95}) in these discharges are 3.0 in #55986, 4.1 in #55935 and 5.2 in #58809. Figure 11 shows the edge temperature, density, pressure gradient, parallel current density and magnetic shear of the above-mentioned three discharges. The edge pressure gradient and current density increase with increasing q_{95}.

Figure 12 shows the α–shear diagrams at $\psi = 0.98$ for the three discharges and the stability limits associated with them. The $n = \infty$ ballooning mode stability boundary is the same for all the discharges, but there is a marked difference in the low- to intermediate-n mode stability. When q_{95} is increased, both the operational point and the low- to intermediate mode stability boundary shift to a higher value of α. Since the normalization of α is neutral to a change in the toroidal magnetic field ($\alpha \sim q^2/B^2$), the absolute value of the stable pressure gradient can also be increased with increase in the edge safety factor.

In addition to the analysis of experimental plasmas, we studied the effect of the edge safety factor by using one of the above-mentioned plasma profiles (#55935), and by adjusting the toroidal field in the equilibrium reconstruction to give the same values of the edge safety factor as in the above experimental scan ($q_{95} = 3.0$, 4.1 and 5.2). Figure 13 illustrates the results of the stability analysis. Unlike in the scan using experimental profiles from different discharges, in this scan the low- to intermediate-n stability boundary is unaffected by the variation in the edge safety factor. Instead, the second stability access for the high-n ballooning modes widens with the increase of the toroidal field. The reason for the apparent discrepancy between the
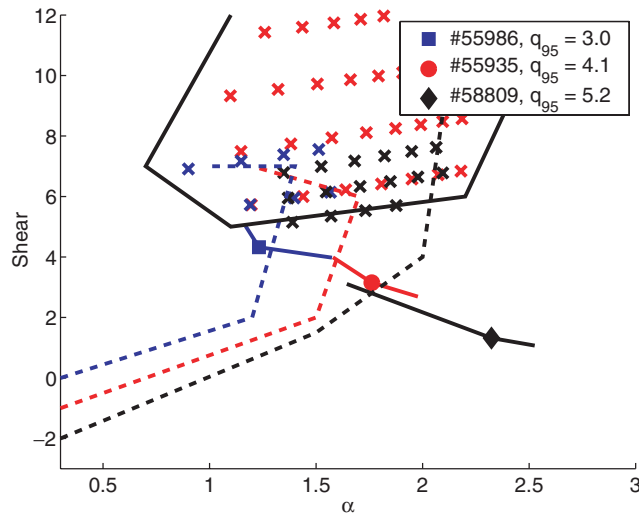
Figure 12. The α–shear stability diagram at $\psi = 0.98$ for three values of q_{95}. The dashed lines show the low- to intermediate-n stability boundaries. For clarity, the labels of the most unstable mode number are not plotted. The solid line and the crosses show the $n = \infty$ ballooning mode boundary. The symbols with error bars show the experimental values of α and shear.
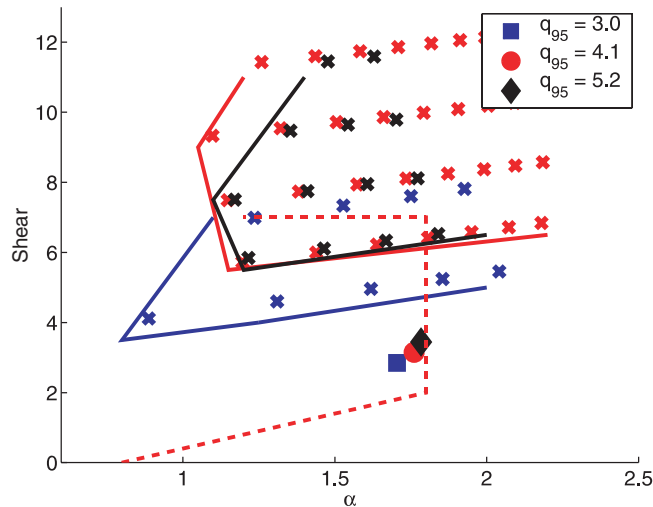

Figure 13. The α–shear stability diagram at $\psi = 0.98$ for the discharge #55935 with a modified toroidal magnetic field in the equilibrium reconstruction to vary q_{95}. The dashed line shows the low- to intermediate-n stability boundaries that applies to all equilibria. The solid lines and the crosses represent the $n = \infty$ ballooning mode unstable region for $q_{95} = 3.0$ (blue), $q_{95} = 4.1$ (red) and $q_{95} = 5.2$ (black). The square, circle and diamond symbols show the operational point values of shear and α of the respective equilibrium.

two stability analysis results is that, in the equilibria calculated using experimental profiles, the current density just inside the pedestal region ($0.9 < \psi < 0.95$) decreases with increasing q_{95}, but with fixed profiles and varying toroidal magnetic field the current in this region does not change. Since the low-n modes extend to this region, the decreased current improves the stability against these modes. Consequently, the stability boundary shifts to higher values of α.

The increasing edge safety factor has very little effect on the radial extent of the unstable mode. This applies to both analyses described above. Therefore, the smaller and more frequent ELMs in high-q_{95} plasmas cannot be explained by the changes in the mode structure of the triggering instability.

4. Summary and conclusions

We analysed the edge stability of a wide range of well-diagnosed JET discharges, using the experimental profile data in the equilibrium reconstruction. During a single Type I ELM cycle, the plasma edge stability changes considerably. Right after the ELM, the edge is deeply stable against the low- to intermediate-n peeling–ballooning modes. On the other hand, it is close to the $n = \infty$ ballooning mode stability limit. As the pressure gradient steepens and the edge bootstrap current builds up, the plasma moves deeper into the second stable region against the $n = \infty$ ballooning modes. Eventually, with a steep enough pressure gradient and high enough current density, the plasma reaches the low- to intermediate-n stability limit and an ELM is triggered. In the stability analysis, the plasma was found to be crossing this stability limit just before an ELM. The mode structure of the ELM triggering instability extends radially across the entire pedestal. The low- to intermediate instability as a trigger for Type I ELMs agrees with the results from similar analyses of experimental plasmas in other tokamaks [6–8].

In plasmas with Type III ELMs, not enough bootstrap current is driven in the edge region due to the high collisionality. Because of this, the edge shear stays high and the plasma does not access second stability against the $n = \infty$ ballooning modes. This leads to a significantly lower edge pressure gradient than in Type I ELMy plasmas. Since the Type III ELMy plasmas are far from the low- to intermediate-n peeling–ballooning mode stability boundary, it is unlikely that they are triggered by the same mechanism as the Type I ELMs.

The stability analysis of the power and gas puffing scans showed that the transition from the Type III to Type I ELMs, either by increasing the heating power or by lowering the gas puffing rate, enables the plasma to enter the second stability region for the $n = \infty$ ballooning modes. The plasma then becomes destabilized by the bootstrap current driven low- to intermediate-n peeling–ballooning mode.

In the discharges where the edge safety factor was increased, the low-n peeling–ballooning mode stability limit is shifted to a higher value of the normalized pressure gradient α. The improved stability enables the achievement of steeper edge pressure gradients before the ELM is triggered. However, the toroidal mode number or the radial mode structure of the ELM triggering instability does not change with variation in the edge safety factor.

Acknowledgments

Appendix. Experimental profiles

The experimental data (after radial shifts for some diagnostics) with fitted curves used in the equilibrium reconstruction for all analysed JET discharges are shown in figures 14–20 (except for #55937 that is already shown in figure 2) and tables A2 and A3. Table A1 shows the radial shifts of the diagnostics used in the fitting.
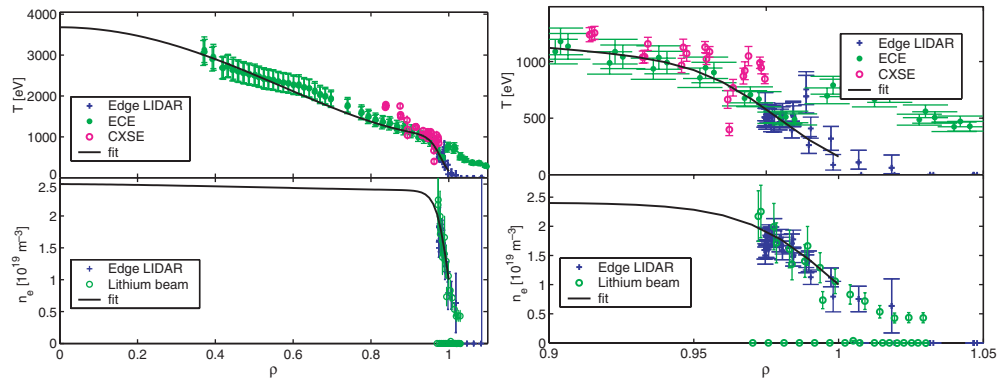
Figure 14. A fitting of the radial temperature and density profiles in the entire plasma and in the edge region for the pulse #55925. Three time points (59.877, 60.877 and 61.186 s) of the experimental profiles have been used because the discharge has Type III ELMs. In this discharge, the core LIDAR data for the above-mentioned time points are not available. Instead, flat density in the core is assumed. The core temperature is fitted using ECE.
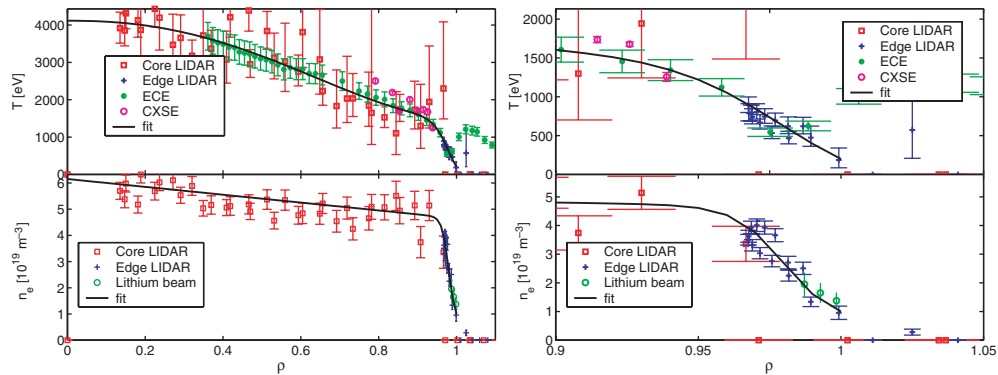

Figure 15. A fitting of the radial temperature and density profiles in the entire plasma and in the edge region for the pulse #55933 at 63.127 s.
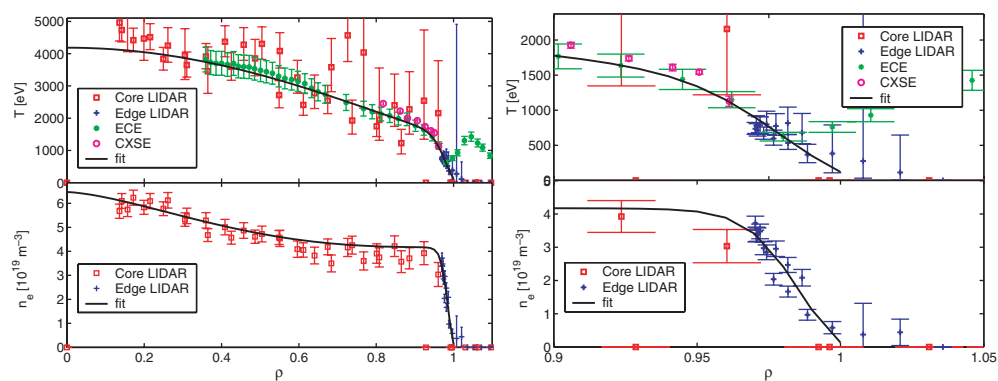

Figure 16. A fitting of the radial temperature and density profiles in the entire plasma and in the edge region for the pulse #55934 at 63.130 s.
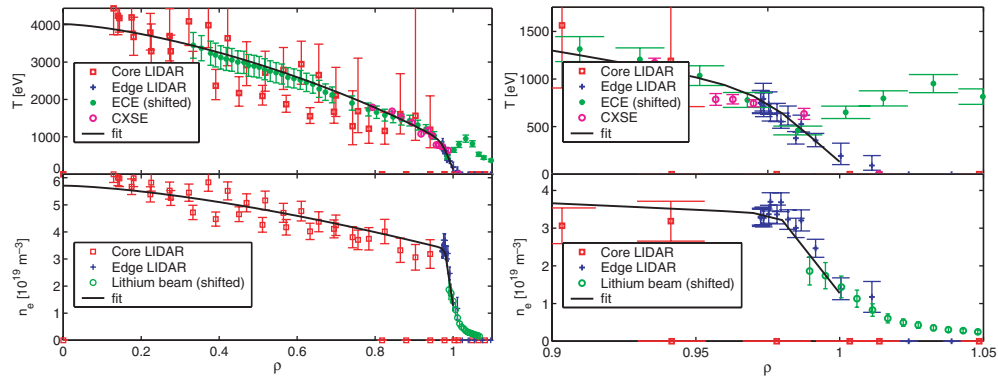
Figure 17. A fitting of the radial temperature and density profiles in the entire plasma and in the edge region for the pulse #55935 at 63.126 s.
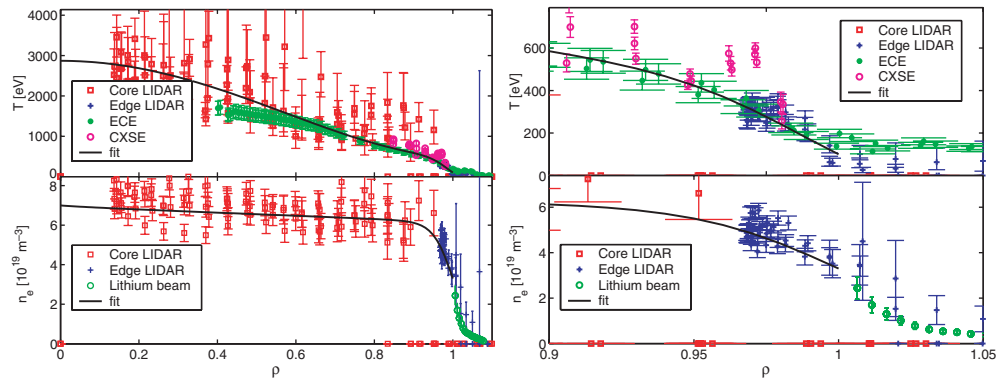

Figure 18. A fitting of the radial temperature and density profiles in the entire plasma and in the edge region for the pulse #55953. Three time points (60.189, 61.143 and 62.174 s) of the experimental profiles have been used because the discharge has Type III ELMs.
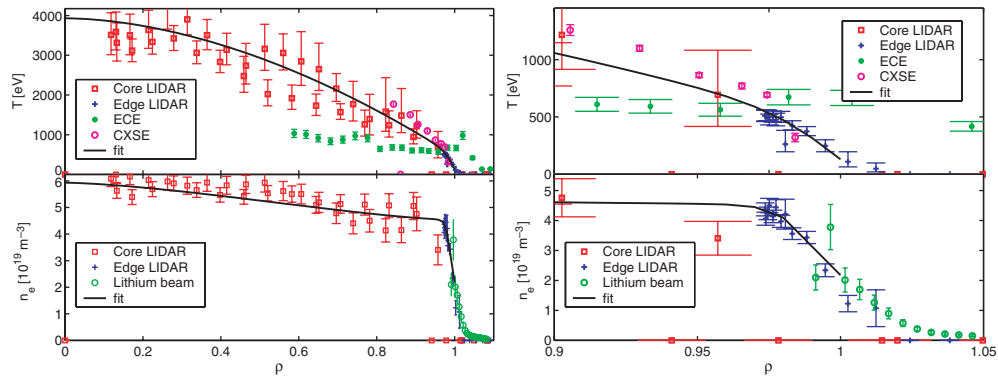

Figure 19. A fitting of the radial temperature and density profiles in the entire plasma and in the edge region for the pulse #55986 at 59.626 s. ECE data cannot be used due to the low magnetic field, and are ignored in the fitting.
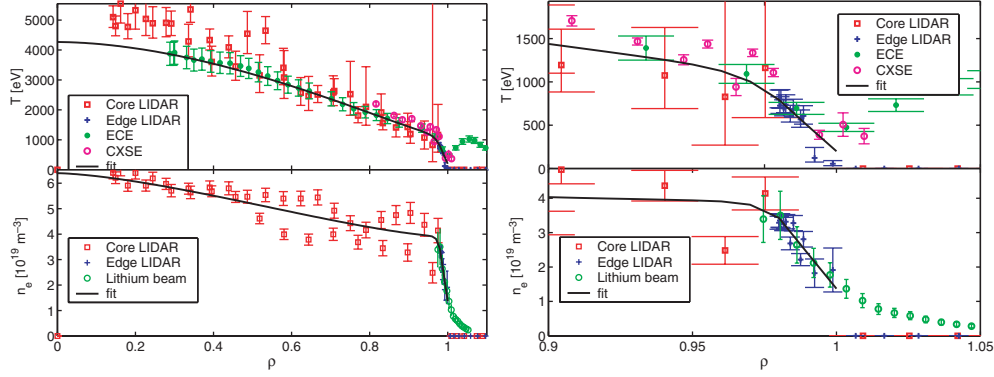
Figure 20. A fitting of the radial temperature and density profiles in the entire plasma and in the edge region for the pulse #58809 at 57.126 s.

Table A1. Radial shifts on the outboard midplane used for the diagnostics.

Discharge	Diagnostic	Radial shift [% toroidal flux, ρ]
#55925	ECE	4.0
#55933	ECE	4.5
#55933	Lithium beam	1.7
#55934	ECE	3.5
#55934	Lithium beam	2
#55935	ECE	5.5
#55935	Lithium beam	1.2
#55937	ECE	4.0
#55937	Lithium beam	0.9
#55953	ECE	4.7
#55953	Lithium beam	1.0
#55986	Edge LIDAR	−1.0
#55986	ECE	5.5
#55986	Lithium beam	0.5
#58809	ECE	3.5
#58809	Lithium beam	1.2

Table A2. Fitting parameters used for the T_e profiles in equations (1). The unit for T_0, T_{ped} and T_{sep} is keV.

Discharge	T_0	T_{ped}	T_{sep}	a_T	b_T	c_T	d_T
#55925	2.65	0.55	0.48	2.0	2.0	0.03	0.98
#55933	2.6	0.9	0.62	2.3	2.0	0.04	0.98
#55934	2.7	0.9	0.58	2.0	1.3	0.035	0.98
#55935	3.3	0.4	0.32	1.5	0.9	0.02	0.99
#55937	3.25	0.65	0.31	1.4	1.0	0.04	0.99
#55953	2.35	0.35	0.17	2.0	2.0	0.05	0.99
#55986	3.5	0.33	0.13	1.8	1.0	0.025	1.0
#58809	3.2	0.58	0.47	1.8	1.2	0.02	0.99

Table A3. Fitting parameters used for the n_e profiles in equation (2). The unit for n_0, n_{ped} and n_{sep} is 10^{19} m^{-3}.

Discharge	n_0	n_{ped}	n_{sep}	a_n	b_n	c_n	d_n
#55925	0.1	1.4	1.0	1.5	1.5	0.032	1.0
#55933	1.5	2.0	2.65	1.0	1.0	0.017	0.98
#55934	3.3	2.4	1.77	1.5	3.2	0.018	0.985
#55935	2.4	1.1	2.31	1.5	1.0	0.0088	0.99
#55937	2.05	2.25	1.0	1.5	1.0	0.01	0.99
#55953	0.9	2.8	3.3	0.8	0.8	0.05	1.0
#55986	1.4	1.4	3.13	1.5	1.5	0.012	0.99
#58809	2.5	1.5	2.4	1.5	1.5	0.012	0.99

References

[1] Leonard A W *et al* 1999 *J. Nucl Mater.* **266–269** 109
[2] Loarte A *et al* 2002 *Plasma Phys. Control. Fusion* **44** 1815
[3] Saibene G *et al* 2002 *Plasma Phys. Control. Fusion* **44** 1769
[4] Connor J W *et al* 1998 *Phys. Plasmas* **5** 2687
[5] Snyder P B *et al* 2002 *Phys. Plasmas* **9** 2037
[6] Saarelma S *et al* 2000 *Plasma Phys. Control. Fusion* **42** A139
[7] Snyder P B *et al* 2004 *Nucl. Fusion* **44** 320
[8] Lao L L *et al* 2001 *Nucl. Fusion* **41** 295
[9] Saibene G *et al* 1999 *Nucl. Fusion* **39** 1133
[10] Suttrop W *et al* 2002 *Phys. Plasmas* **9** 2103
[11] Kallenbach A *et al* 2004 *Plasma Phys. Control. Fusion* **46** 431
[12] Gowers C, Beurskens M and Nielsen P 2000 *J. Plasma Fusion Res.* **76** 874
[13] Kempenaars M *et al* 2003 *30th EPS Conf. on Controlled Fusion and Plasma Physics (St Petersburg)* vol 27A (ECA)
[14] Salzmann H 1989 JET-R(89)07
[15] Bartlett D V *et al* 1992 *8th Joint Workshop on Electron Cyclotron Emission and Electron Cyclotron Resonance Heating (Gut-Ising, Germany, 1992)*
[16] Porte L, Bartlett D V, Campbell D J and Costley A E 1991 *18th EPS Conf. on Plasma Physics and Controlled Fusion (Berlin)*
[17] Cennachi G and Taroni A 1998 JET-IR(88)03
[18] Lao L *et al* 1985 *Nucl. Fusion* **25** 1611
[19] Mihailovskii A B *et al* 1997 *Plasma Phys. Rep.* **23** 844
[20] Huysmans G T A, Goedbloed J P and Kerner W O K 1991 *Computational Physics: Proc. Int. Conf. (Amsterdam, 1991)* (Singapore: World Scientific) p 371
[21] Perez C P *et al* 2002 *29th EPS Conf. on Plasma Physics and Controlled Fusion (Montreux)* vol 26B (ECA) P-1.023
[22] Perez C P *et al* 2004 *Nucl. Fusion* **44** 609
[23] Lonnroth J-S *et al* 2003 *Plasma Phys. Control. Fusion* **45** 1689